Investigations of the Mn–Ni–Sm ternary system by means of anomalous X-ray diffraction, X-ray absorption and DFT calculations

Nicolas Madern, Judith Monnier, Jean-Claude Crivello, Junxian Zhang, Karine Provost, Valérie Paul-Boncour, Solenn Réguer, Dominique Thiaudière, Michel Latroche

Investigations of the Mn–Ni–Sm ternary system by means of anomalous X-ray diffraction, X-ray absorption and DFT calculations

Nicolas Madern[1], Judith Monnier[*,1], Jean-Claude Crivello[1], Junxian Zhang[1], Karine Provost[1], Valérie Paul-Boncour[1], Solenn Réguer[2], Dominique Thiaudière[2], Michel Latroche[1,†]

[1]Univ. Paris-Est Créteil, CNRS, ICMPE, UMR7182, F-94320, Thiais, France

[2]Synchrotron SOLEIL, L'Orme Des Merisiers, départementale 128, 91190 Saint-Aubin, France

*Corresponding author (judith.monnier@cnrs.fr, ICMPE, 2-8 rue Henri Dunant, 94320 Thiais, France)

Abstract

Various applications benefit from the use of compounds combining lanthanides and 3*d* metals because of their fundamental physicochemical properties. To select the best systems and to overcome the criticality of raw materials or geopolitical tension, a better understanding of the binary, ternary and even quaternary systems is needed. The present work focuses on the ternary Mn-Ni-Sm system, which is particularly interesting for energy storage applications as it forms hydrogen absorbing intermetallic compounds. The fruitful combination of standard X-ray diffraction, anomalous X ray diffraction close to the Mn 3*d* edge, X-ray absorption XANES, electron probe micro-analysis and first-principles calculations provides a better understanding of the physicochemical properties and phase equilibrium of this ternary system. In particular, the atomic substitution of Mn atoms in the Ni sites has been investigated for the stacking AB_2/AB_5 $Sm_2Mn_yNi_{7-y}$ system. The Mn atoms substitute preferentially in the AB_5 sub-units, whereas Sm vacancies are observed in the AB_2 sub-units inducing an antagonist variation in cell volume units. In the $SmMn_yNi_{12-y}$ system, the preferential localization of Mn atoms has been highlighted in site 8*i* for the $SmMn_4Ni_8$ compound.

Keywords

Intermetallic; Ternary alloy; Anomalous X ray diffraction; Crystal structure; DFT; Ssynchrotron

† Deceased author

Introduction

Compounds associating lanthanides and 3*d* metals are widely studied due to their fundamental physicochemistry leading to attractive properties for diverse applications such as magnetism [1,2], magnetocaloric effect [3,4], permanent magnets [5], Ni-*M*H batteries [6] or solid-state hydrogen storage [7]. Beside these technological developments, these materials face some compositional issues related to their Critical Raw Materials (CRM) character or geopolitical tensions [8].

These issues can be overcome by the possibilities of replacing one rare earth by another or introducing a third lighter elements. However, these strategies must be based on an increased knowledge of the binary and ternary (even quaternary) systems. As an example, the Co-Sm system has been widely investigated due to its excellent magnetic properties forming permanent magnets ($SmCo_5$, Sm_2Co_{17}) [5]. Besides, the Mn-Ni-Sm system brings increasing interest as it contains intermetallic compounds forming hydrides for energy storage applications. This ternary system [9] offers a rich chemistry with nine Ni-Sm binary phases, one Mn-Sm and one Mn-Ni binary phases, completed by large pseudo-binary extensions in the iso-Sm line ternary domain. In addition, one ternary phase is reported, the $SmMn_4Ni_8$.

Some unexpected chemical and structural behaviors are reported for Mn-Ni-Sm system as a function of the composition, such as erroneous stoichiometry, Sm vacancies, anisotropic Ni/Mn distribution, antisites or deviation from the Vegard's law for some Ni/Mn substitution [9–15]. This fact is mainly due to the difficulty to unambiguously resolve the crystal structures as standard X-ray diffraction does not allow to discriminate between Ni and Mn which have a very close electronic configuration. Moreover, the strong neutron absorption of Sm prevents the use of neutron diffraction data. Therefore, in the present work, combination of different techniques i.e. standard X-ray diffraction (XRD), synchrotron anomalous X ray diffraction (AXRD) close to the 3*d* edges, X-ray absorption near edge structure (XANES), Electron Probe Micro-Analysis (EPMA) and first-principles calculations have been combined to get a better understanding of the physicochemical properties and phase equilibrium of systems belonging to the Mn-Ni-Sm ternary (an overview of the investigated compositions is reported in Figure 1.

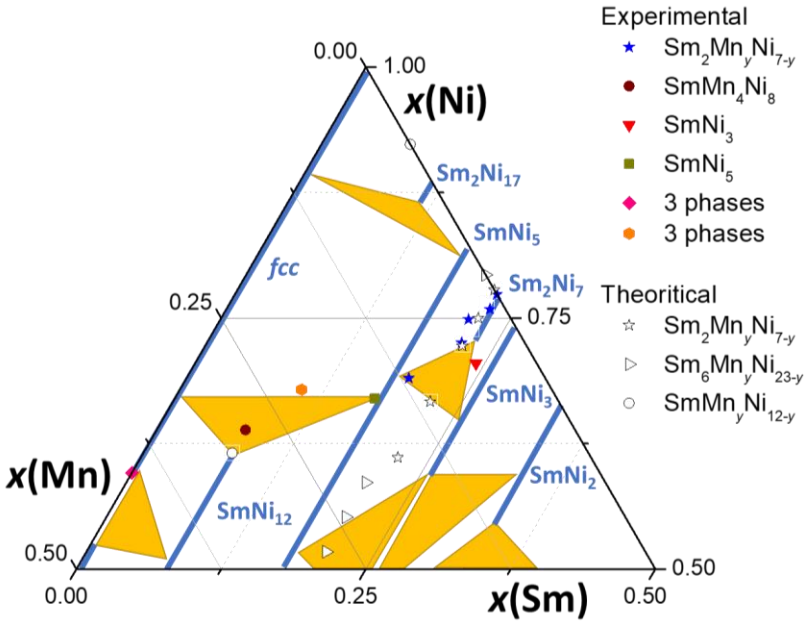

Fig. 1: Isothermal section (400:600°C) of the manganese-nickel-samarium ternary phase diagram (1981 Bodak O.I.), for 0<x(Sm)<0.5, 0< x(Mn)<0.5 and 0.5<x(Ni)<1 with x the molar fraction, superimposed with the compositions $Sm_2Mn_yNi_{7-y}$ (y_{Mn}=0; 0,12; 0,35, 0,49 and 1; blue stars) and $SmMn_4Ni_8$ (brown circle). Observed phases in equilibrium with $Sm_2Mn_yNi_{7-y}$ are shown as red triangles ($SmNi_3$-type, y_{Mn}=0,49) and green square ($SmNi_5$-type, y_{Mn}=1,0). Observed phases in equilibrium with $SmMn_4Ni_8$ are shown as pink diamond (Mn,Ni-type) and orange hexagon (Sm_2Ni_{17}-type). Sm_2O_3 oxides are not shown. It is worth to note that this figure is only for comparison as the temperatures of the phase diagram are different from that of the annealed phases studied in this work. In black empty symbols, some of the first-principles calculated compositions are shown.

Experimental and computational methodologies

All compounds were made from high purity elements: Sm (Alfa Aesar 99.9%), Ni (Praxair 99.95%) and Mn (Alfa Aesar 99.99%). For the $Sm_2Ni_{7-y}Mn_y$ compounds, the elements were first melted in an induction furnace under argon (P_{Ar} ≈ 40 kPa, Linde 99.995%). This step was repeated three times to ensure good homogeneity. Small excess of Sm (3.5 wt.%) and Mn (3 wt.%) were initially added to compensate the losses induced by evaporation during the three melting steps. After induction melting, the ingots were crushed into powder (<100 µm), pressed into 2 g-pellets, wrapped in a tantalum foil, and heat-treated under argon atmosphere in a sealed stainless-steel crucible for 3 days at 800 °C, except for Sm_2Ni_7 which was annealed at 950 °C. For $SmMn_4Ni_8$, the elements were melted in stoichiometric proportion using an induction furnace such as for the previous alloys, the compound was studied as cast. For Sm_6Mn_{23}, the ingot obtained by induction melting was wrapped in a Ta foil and annealed at 800 °C for 2 weeks in a closed silica tube under argon partial pressure. All compounds were finally water quenched to preserve the high temperature structures.

Powdered samples were first characterized by standard laboratory based XRD using a Bruker D8 DAVINCI diffractometer (Cu-K_α radiation) in the range 20 to 80° (2θ) by step of 0.01°. Experimental data were analyzed by the Rietveld method using either FullProf [16] or Topas [17,18] packages. EPMA was performed for all samples with a CAMECA SX-100 to determine their chemical compositions. The samples were first polished with a 3-µm diamond abrasive paste and ethanol solvent on a woven tape.

Combination of XRD, AXRD and XANES at room temperature was performed at the DiffAbs SOLEIL beamline. For each sample, two synchrotron diffraction patterns were collected: one was obtained below the Mn absorption K-edge at a wavelength far away from possible resonant effects (λ = 2.06954 Å using a punctual detector and the other one just below the Mn K-edge (λ = 1.89699 Å) using an energy resolved 1-element SDD (Silicon Drift Detector), the exact wavelength values being determined using a LaB_6 standard reference from NIST. Additional set of patterns were measured at 18 keV (λ = 0.689645 Å) to probe a larger sample thickness. XANES measurements were performed before AXRD, one being as close as possible from the absorption edge to maximize f' contrasts. Due to the high absorption of the samples (μ = 1845 cm^{-1} at 6.52 keV) in the energy range investigated (6.0 < E < 6.7 keV), data were recorded with flat-plate geometry with detection by the total fluorescence yield and energy resolution of 0.5 eV. Samples were crushed mechanically and sieved (<20 µm) in argon atmosphere. They were then pelletized with 5 wt.% of PTFE, fixed on the sample holder, and spun during data collection. The theoretically calculated values for the dispersion correction coefficients f' and f'' can be used with confidence from data bases, as these values for free atoms are a good approximation for intermetallics without covalent bonds. The data treatment was done using a joint Rietveld refinement of the two XRD patterns (at 6 and 6.52 keV) with the Fullprof package [16] and Topas software [17,18]. XANES measurements were performed for all samples with flat-plate geometry. Self-absorption was corrected using Absorbix software [19] taking into account the real elemental compositions as well as measured incidence (10°) and detection (1.15°) angles for the fluorescence detector (4-elements SDD). The Mn energy K-edge, determined by the first inflexion point (maximum of the first derivative) of the Mn foil is at 6540 eV.

The calculations reported in this work are based on the density functional theory (DFT) with and without spin polarization. They have been performed using the projector augmented wave method (PAW) [20], implemented in the Vienna Ab initio Simulation Package (VASP) [21,22]. The exchange-correlation energy of electrons is described in the generalized gradient approximation (GGA) using the Perdew–Burke–Ernzerhof functional parametrization [23]. Traditional potentials have been considered for Ni and Mn. About Samarium, we have used the "ghost-state" treatment "Sm_3", without correcting energy as in the Hubbard type: the *f*-electrons are kept frozen with the core-electrons to provide a valency of 3. After necessary tests to control the stability of the energy convergence, the energy cut-off for the PAWs was set to 600 eV. Brillouin zone sampling was done using a *k*-meshing of 0.05 $Å^{-1}$ points for each primitive cell. A

complete relaxation set (volume cell shape and ionic position) has been done under the condition that residual forces should be smaller than 1 meV.Å^{-1} keeping the initial symmetry. A final self-consistent static calculation was done with the tetrahedron smearing method with Blöchl corrections [24]. For this theoretical work, we have performed systematic calculations considering a compositional range in the three different phases, as represented in Fig. 2: $Sm_2Mn_yNi_{7-y}$ in Ce_2Ni_7 prototype (*hP*36), $P6_3/mmc$ (194), see crystallographic environnements in Fig. SI-1

- $SmMn_yNi_{12-y}$ in $ThMn_{12}$ prototype (*tI*26), I_4/mmm (139), see crystallographic environments in Fig. SI-2
- $Sm_6Mn_yNi_{23-y}$ in Th_6Mn_{23} prototype (*cF*116), $Fm\bar{3}m$ (225), see crystallographic environments in Fig. SI-3

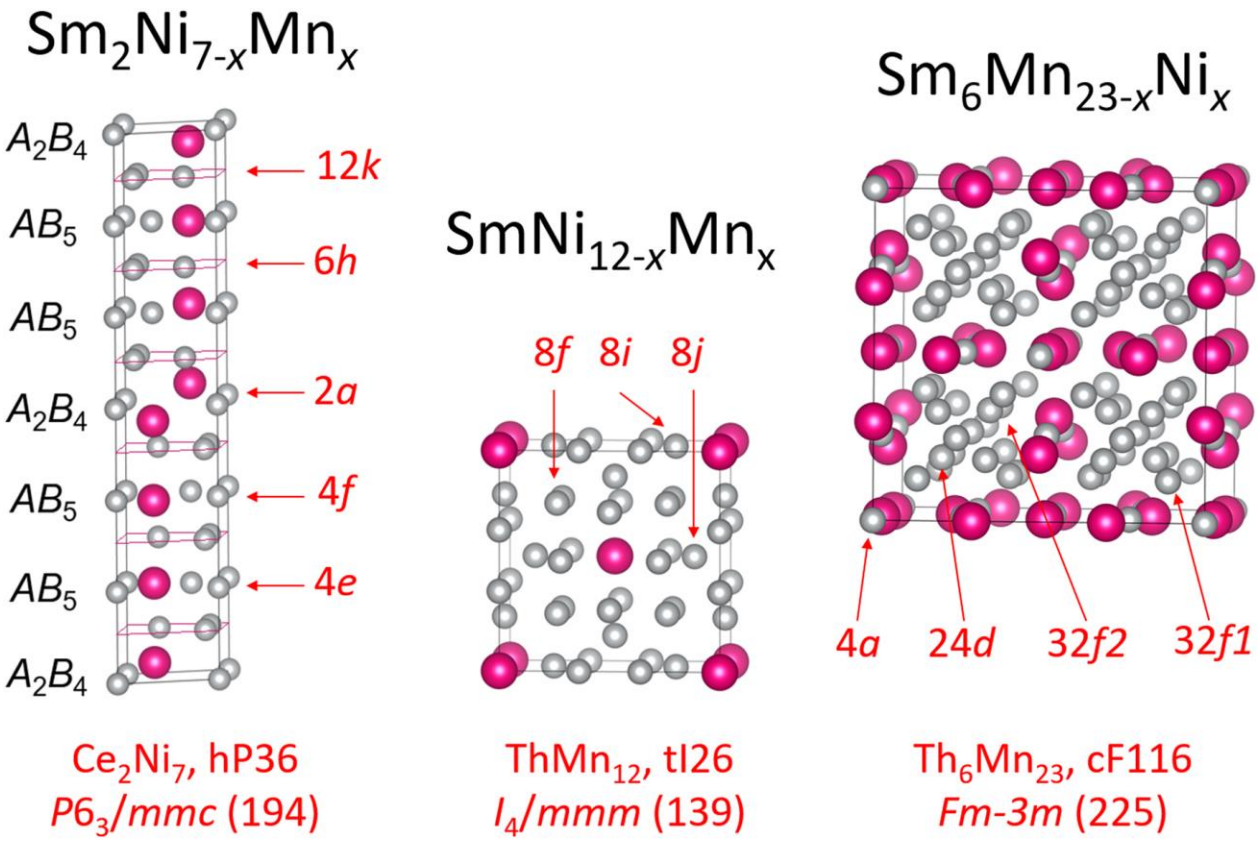

Fig. 2. Crystal structure of $Sm_2Mn_yNi_{7-y}$, $SmMnyNi_{12-y}$ and $Sm_6Ni_{23-y}Mn_y$ compounds. Details of Coordination spheres of each Mn/Ni sites are given in supplementary materials.

Substitution of Mn on Ni sites has been performed considering the ordered distribution of Mn/Ni atoms on each Wyckoff sites by testing several possible orderings for a given composition (only the most stable was kept). The disordering distribution, that could be modelled using supercell was neglected here, since it has been check that there is no energy difference from our preliminary tests, excepted for the solute Mn atom with one equivalent possibility according to each Wyckoff site (See details of coordination sphere in SI-1, SI-2 and SI-3). In fact, the *y*Mn= 1/28 composition of Sm2Ni7−yMny has been investigated considering a solute Mn atom in one individual site of each position in the hexagonal Sm8*B*28 description model. In addition, two Ni-Sm compounds have been considered to verify binaries equilibrium: Sm_2Ni_{17} ($P6_3/mmc$) and $SmNi_5$ (P_6/mmm).

Results

$Sm_2Mn_yNi_{7-y}$

Five compositions have been synthetized for this given stoichiometry with y_{Mn}=0; 0.12; 0.35; 0.49 and 1.0. Compositional analysis made by EPMA are given in Table 1. The 2/7 stoichiometry is indeed observed for the binary system (y_{Mn}=0). However, increasing *y* induces a progressive sub-stoichiometry of the rare earth, attaining 16 % for y_{Mn}=1 (x_{Sm}=1.68; EPMA plot shown in Fig. SI-4). The Sm stoichiometry decreases almost linearly with *y*, except at very low Mn (Fig. 3. Evolution of the Sm stoichiometry (x_{Sm}) as a function of the Mn content (y_{Mn}) for the system Sm2MnyNi7−y obtained by EMPA (open squares) and XRD refinement (blue hexagons for 2H and red triangles for 3R).), for which some abnormal behavior is observed.

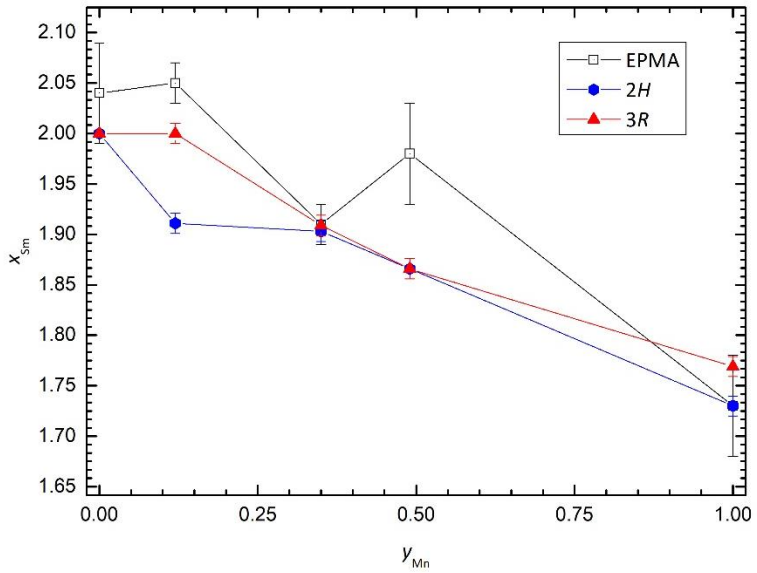

Fig. 3. Evolution of the Sm stoichiometry (x_{Sm}) as a function of the Mn content (y_{Mn}) for the system Sm2MnyNi7−y obtained by EMPA (open squares) and XRD refinement (blue hexagons for 2H and red triangles for 3R).

X-ray diffraction patterns have been recorded for all samples by standard XRD and AXRD. From the data analysis, the different phases present in the samples have been identified. First, for all compounds, small amounts of Sm_2O_3 (either monoclinic *C*2/*m* or cubic *Ia*$\bar{3}$, < 2 wt.% except for y_{Mn} = 1,~10 %) are detected (Table 1). Beside this minor phase, the two polymorphic phases, (2*H* hexagonal Ce_2Ni_7-type $P6_3/mmc$ space group named *H* hereafter, and 3*R* rhombohedral Gd_2Co_7-type, *R*$\bar{3}$*m* named *R* hereafter) are mainly observed for $0 \le y_{Mn} < 0.49$. For higher y_{Mn} values, the diagrams of Figure 1 show the appearance of the pseudo-binary $Sm(Ni,Mn)_3$ phase (y_{Mn} = 0.49; $PuNi_3$-type, *R*$\bar{3}$*m*)) and $Sm(Ni,Mn)_5$ phase (y_{Mn} = 1.0; $CaCu_5$-type *P*6/*mmm*). Despite some differences between standard XRD and AXRD ones as listed in Table 1, the phase quantities observed by the two methods are in rather good agreement, keeping in mind that the analyses were done on different parts of powder from the same samples. For the 2 polymorphic phases with 2/7 stoichiometry, the *H* over *H*+*R* ratio is shown in Fig. -a to highlight the proportion of the 2:7 *H* polymorph compared to the whole 2:7 structure (*H*+*R*). A. A linear relationship between this ratio and the Mn amount y_{Mn} is clearly seen, indicating that the *H* polymorph becomes predominant for higher y_{Mn} values. Besides, the linear correlations of *H*/(*H*+*R*) with x_{Sm} is also observed (Fig. -b). Complementary set of diffraction patterns has been recorded at a higher energy of 18 keV (λ = 0.689645 Å), as a larger thickness of sample will be measured and possible surface effects more negligible. As similar crystallographic results were obtained compared to lower energy (6.5 KeV) it confirms that the structural results are not dependent on the probed sample thickness.

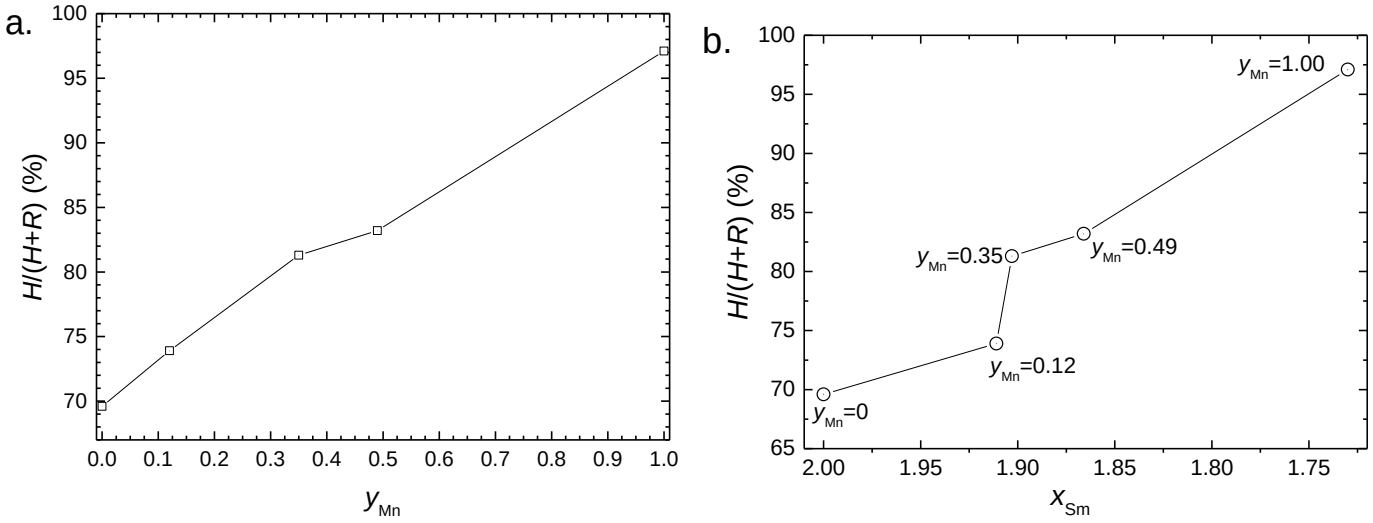

***Fig. 4**: Evolution of (a) the H/(H+R) ratio (in %) as a function of the Mn content (y_{Mn}) and (b) the Sm occupancy content (x_{Sm}, labels in the figure stand for y_{Mn} values) for the system $Sm_2Mn_yNi_{7-y}$, obtained by X-ray diffraction analysis. Note that the x-axis decreases from x_{Sm}=2.00 to 1.70 for a better comparison with y_{Mn}.*

Thanks to AXRD, it was possible to investigate the atomic distribution of Mn atoms in the Ni sublattices for the $Sm_2Mn_yNi_{7-y}$ system. This analysis was mostly made for the 2*H* hexagonal Ce_2Ni_7-type phase as it is the main phase in all samples. Distribution of Mn over Ni sites is given in Table 2 for all compositions, as well as the refined Sm stoichiometry. Regarding the rare earth, it is found that the sub-stoichiometry observed by EMPA is related to the presence of vacancies at the 4f_1 Wyckoff position, *i.e.*, the Sm-site lying in the AB_2 sub-unit.

As concerns manganese, no Mn atoms were found in the 4*f* position and few of them in 2*a* and 4*e* (only for y_{Mn} = 0.49). Mn is mainly located in positions 6*h* in the AB_5 sub-unit and 12*k* lying at the border between the sub-units AB_5 and AB_2. As a general trend, the Mn atoms are occupying AB_5 sub-units (assuming that 12*k* can be accounted as AB_5). Accordingly, one can assume a linear filling of AB_5 sub-units as shown in Fig.
.

Table 1: Chemical and structural analysis of the compositions studied by EPMA, AXRD and XRD for the Mn-Ni-Sm ternary system.

System	EPMA	Phase	%Phase AXRD	%Phase XRD	Cell parameters (Å)
$Sm_2Mn_yNi_{7-y}$ y_{Mn}=0	$Sm_{2.04(5)}Ni_{6.97(5)}$	Ce_2Ni_7-type (2*H*) $P6_3/mmc$	70(1)	77(1)	*a* = 4.9782(4) *c* = 24.308(2)
		Gd_2Co_7-type (3*R*) $R\bar{3}m$	30(1)	23(1)	*a* = 4.9772(7) *c* = 36.474(6)
$Sm_2Mn_yNi_{7-y}$ y_{Mn}=0.12	$Sm_{2.05(2)}Mn_{0.12(2)}Ni_{6.83(3)}$	Ce_2Ni_7-type (2*H*) $P6_3/mmc$	73(1)	77(1)	*a* = 4.9903(3) *c* = 24.348(1)
		Gd_2Co_7-type (3*R*) $R\bar{3}m$	26(1)	22(1)	*a* = 4.9884(5) *c* = 36.530(6)
		Sm_2O_3 $Ia\bar{3}$	1(1)	1(1)	fixed*

$Sm_2Mn_yNi_{7-y}$ y_{Mn}=0.35	$Sm_{1.91(2)}Mn_{0.33(4)}Ni_{6.67(4)}$	Ce_2Ni_7-type (2*H*) $P6_3/mmc$	79(1)	78(1)	*a* = 4.9948(2) *c* = 24.341(1)
		Gd_2Co_7-type (3*R*) $R\bar{3}m$	18(1)	18(1)	*a* = 4.9927(5) *c* = 36.516(9)
		Sm_2O_3 $Ia\bar{3}$	2(1)	1(1)	fixed*
		Sm_2O_3 C2/*m*	1(1)	3(1)	fixed*
$Sm_2Mn_yNi_{7-y}$ y_{Mn}=0.49	$Sm_{1.98(5)}Mn_{0.49(4)}Ni_{6.52(7)}$	Ce_2Ni_7-type (2*H*) $P6_3/mmc$	47(1)	58(1)	*a* = 5.0065(3) *c* = 24.401(1)
		Gd_2Co_7-type (3*R*) $R\bar{3}m$	9(1)	10(1)	*a* = 5.0124(8) *c* = 36.595(5)
	$Sm_{0.97(4)}Mn_{0.21(2)}Ni_{2.82(4)}$	$PuNi_3$-type (3*R*) $R\bar{3}m$	43(1)	31(1))	*a* = 5.0173(3) *c* = 24.551(3)
		Sm_2O_3 $Ia\bar{3}$	1(1)	1(1)	fixed*
$Sm_2Mn_yNi_{7-y}$ y_{Mn}=1,00	$Sm_{1,73(5)}Mn_{1.06(8)}Ni_{6.21(6)}$	Ce_2Ni_7-type (2*H*) $P6_3/mmc$	88(2)	67(1)	*a* = 4.9991(3) *c* = 24.296(1)
		Gd_2Co_7-type (3*R*) $R\bar{3}m$	0	10(1)	*a* = 4.9963(7) *c* = 36.365(6)
	$Sm_{1.01(1)}Mn_{0.92(2)}Ni_{3.92(3)}$	$CaCu_5$-type *P*6/*mmm*	2(1)	14(1)	*a* = 4.948(5) *c* = 4.45(8)
	$Sm_{2.01(7)}O_{3.0(9)}$	Sm_2O_3 $Ia\bar{3}$	10(1)	9(1)	fixed*
$SmMn_4Ni_8$	$SmMn_{3,7(2)}Ni_{8,3(1)}$	$ThMn_{12}$-type *I*4/*mmm*	86(1)	68(1)	*a* = 8.4888(4) *c* = 4.7699(3)
	$Sm_2Mn_{4,1(1)}Ni_{12,9(2)}$	Th_2Ni_{17}-type $P6_3/mmc$	5(1)	20(1)	*a* = 8.497(2) *c* = 8.441(4)
	$Ni_{59(1)}Mn_{40(1)}$	$Ni_{60}Mn_{40}$ $Im\bar{3}m$	5(1)	7(1)	*a* = 2. 9721(2)
		Sm_2O_3 C2/*m*	4(1)	5(1)	fixed*
Sm_6Mn_{23}	$Sm_{5.9(1)}Mn_{23.1(1)}$	Th_6Mn_{23}-type $Fm\bar{3}m$		95(1)	*a* = 12.5896(2)
	$Mn_{92.3(1)}Sm_{7.7(1)}$	αMn-type $I\bar{4}3m$		5(1)	*a* = 9.091(4)

*Sm_2O_3 ($Ia\bar{3}$) *a* = 10.9277 Å; Sm_2O_3 (C2/m) a = 14.1916, b = 3.6248 Å, c = 8.8557 Å, β = 99.943°

Besides the site occupancies of Sm, Ni and Mn, XRD analysis also gives access to atomic positions. In the particular case of the stacking structure, refinement of the *z* positions of the Ni(Mn) atoms, combined with the cell parameters, allows to calculate the total cell and individual volumes of each stacking sub-units, AB_5 and AB_2, respectively. Such analysis is given in Fig. 6. Cell parameters behave similarly for the 2*H* and 3*R* polymorphs (Fig. 6-a). However, they do not show a linear behavior as a function of y_{Mn}, as it can be expected from a simple Vegard's law [25]. Cell parameters increase with y_{Mn} up to 0.5 then decrease up to y_{Mn} = 1. Accordingly, the cell volume of the 2*H* phase increases regularly between $0 \leq y_{Mn} \leq 0.49$ to reach a maximum then decreases in the range $0.49 \leq y_{Mn} \leq 1.00$ (Fig. 6-b). This is not the case for the individual sub-unit volumes that show different behaviors. V_{AB5} increases smoothly between $0 \leq y_{Mn} \leq 0.49$, reaching a maximum and remains constant up to y_{Mn} = 1.00. The behavior of V_{AB2} is more complex with a pseudo-minimum between $0.25 \leq y_{Mn} \leq 0.45$, then a maximum at y_{Mn} = 0.49, followed by a significant decrease for $0.49 \leq y_{Mn} \leq 1.00$ (Fig. 6-c).

Table 2: Sm and Mn distribution in Wyckoff sites and sub-unit volumes (AB_2 and AB_5) for $Sm_2Mn_yNi_{7-y}$ with 2H hexagonal Ce_2Ni_7-type structure (grey background highlights the AB_2 sub-unit).

y_{Mn}		0	0.12	0.35	0.49	1.00
Sm 4f_1	AB_2	1	0.911(8)	0.903(8)	0.866(9)	0.730(9)
Sm 4f_2	AB_5	1	1	1	1	1
Ni 2*a*	AB_2				0.02(6)	
Ni 4*e*	AB_5				0.10(3)	
Ni 4*f*	AB_5					
Ni 6*h*	AB_5		0.07(2)		0.25(2)	0.40(2)
Ni 12*k*	AB_5/AB_2		0.006(12)	0.11(2)		0.13(1)
Sum Occ_{Sm}*		2	1.91(1)	1.90(1)	1.87(1)	1.73(1)
Sum Occ_{Mn} **		0	0.12(7)	0.33(5)	0.49(9)	1.00(7)
Occ_{Mn} in AB_5	AB_5	0	0.12(7)	0.33(5)	0.48(6)	1.00(7)
Occ_{Mn} in AB_2	AB_2	0	0	0	0.01(3)	0
VAB_5 (Å^3)	AB_5	84.9(4)	86.0(1)	86.6(1)	87.2(2)	81.2(2)
VAB_2 (Å^3)	AB_2	91.0(7)	90.5(3)	89.7(3)	90.5(3)	88.7(4)
VTotal (Å^3)		521.7(1)	525.1(1)	525.9(1)	529.7(1)	525.8(1)

* Sm occupancy: Sum Occ_{Sm}= (4*Sm4*f*1 + 4*Sm4*f*2)/4

** Mn occupancy: Sum Occ_{Mn} = (2*Ni 2*a* + 4*Ni4*e* + 4*Ni4*f* + 6*Ni6*h* + 12*12*k*)/4

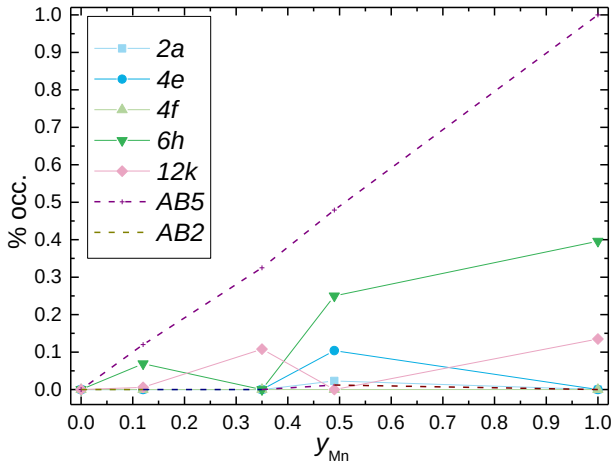

Fig. 5: *Mn for Ni distribution obtained by AXRD analysis for the different Wyckoff positions (%) and Mn occupancies in AB_5 and AB_2 sub-units for $Sm_xMn_yNi_{7-y}$ with 2H hexagonal Ce_2Ni_7-type structure as a function of the Mn content y_{Mn}.*

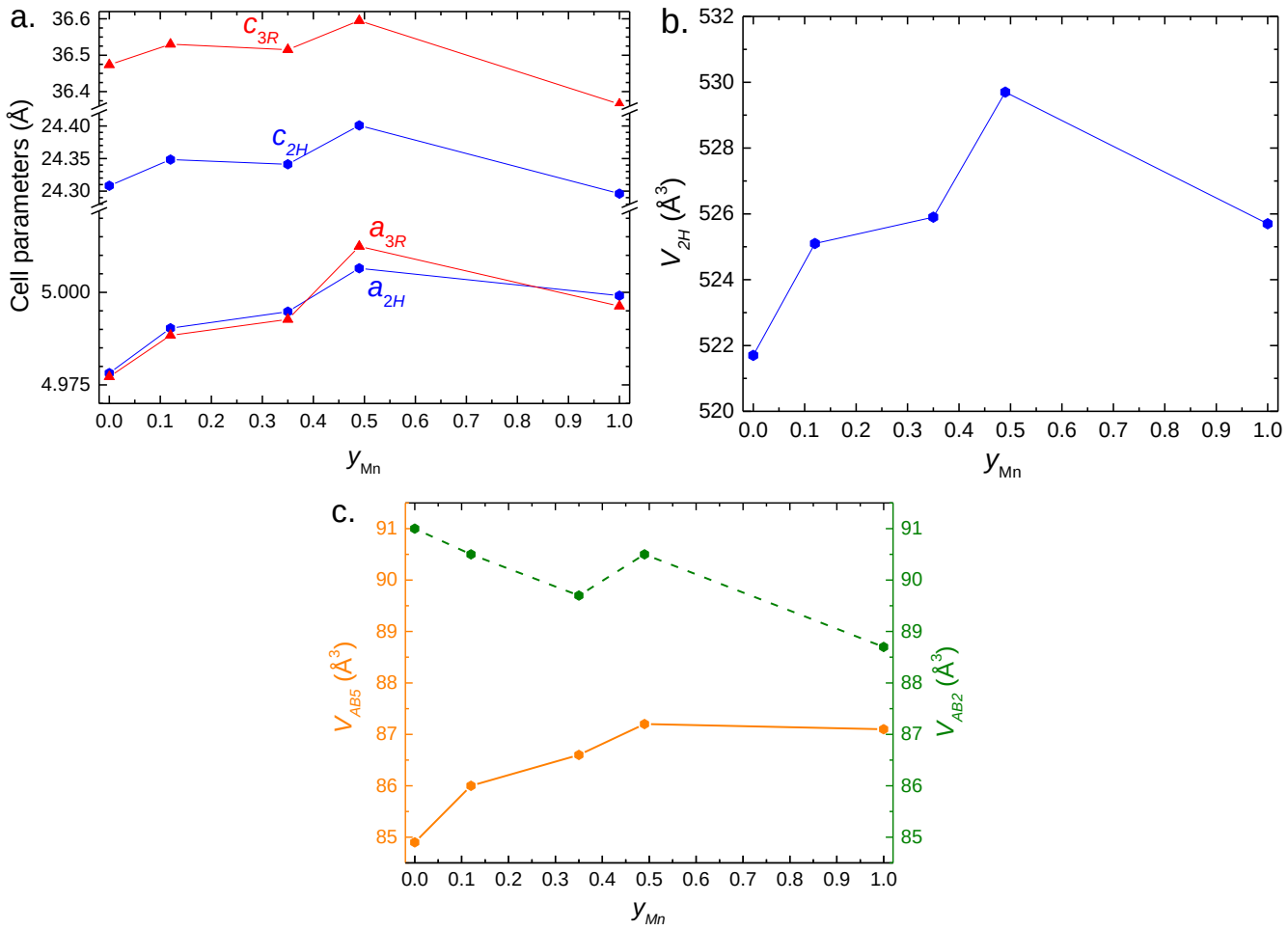

Fig. 6: Evolution of (a.) the cell parameters of 2H and 3R polymorphs, (b.) the full cell volume of the 2H phase and (c.) the sub-unit volumes AB_5 (full orange line) and AB_2 (dashed green line) of the 2H phase as a function of the Mn content y_{Mn} for the system $Sm_xMn_yNi_{7-y}$.

The cell volumes can also be affected by the Sm composition, as sub-stoichiometry might induce volume contraction effects. Thus, the same analysis can be done as a function of x_{Sm}, *i.e.,* the sub-stoichiometry in rare earth (Fig. SI-5). From $x_{Sm} = 2$ to 1.85, the total volume increases to a maximum, then decreases down to 1.72, in a similar way than with y_{Mn}. For individual sub-units, V_{AB5} increases with x_{Sm} down to 1.85, and then remains almost constant. Again, V_{AB2} shows more striking features with a general decrease as a trend, but a local minimum around $x_{Sm} = 1.9$.

The DFT investigation on $Sm_2Mn_yNi_{7-y}$ was only done on the hexagonal 2*H* phase. In fact, preliminary calculations showed no distinct energy difference with 3*R* type, in agreement with other investigations on stacking's phases such as $(La,Y)_2Ni_7$ phase [26] or $(La,Mg)_2Ni_7$ [27]. From the total energy difference of compounds with energies of pure elements in their reference state (dhcp, A12 and fcc spin-polarized for Sm, Mn and Ni respectively), the heat of formation, ΔH^{for}, is calculated and represented in Fig. -a. Whereas the Mn in 6*h* site seems to be favorable without spin polarization, the magnetic contribution is slightly changing the preference to 4*a* at concentration $y_{Mn} = 1$. One may note that all sites present the same coordination number of 12 and only the nature of neighbors is changing.

The relaxed volume and *c/a* ratio, corresponding to the most stable compounds on the DFT ground-state, are shown in Fig. -b. Whereas volume is increasing continuously with y_{Mn}, the *c/a* ratio presents a V-shape, but it may be a misreading from the metastable $y_{Mn} = 3$ limit-compound.

The electronic structure in both spin population is given for Sm_2Ni_7, Sm_2Ni_6Mn Sm_2Mn_7 in supplementary information (See Figure Fig. SI-6). The density of state (DOS) of Sm_2Ni_7 is very similar to those of La_2Ni_7: a main structure is dominated by Ni-3*d* bands and the emergence of ferromagnetism is explained by the filling of the majority states from electrons of minority bands. By increasing the value of y_{Mn} (Mn composition), we can see a progressive depopulation of the main *d*-structure, accompanied by a progressive raising of the structure of empty state structure after the Fermi level (Mn presents 3 electrons less than Ni). The Mn contribution is ferromagnetic with a strong electronic transfer from minority to majority bands whatever the occupied Wyckoff site.

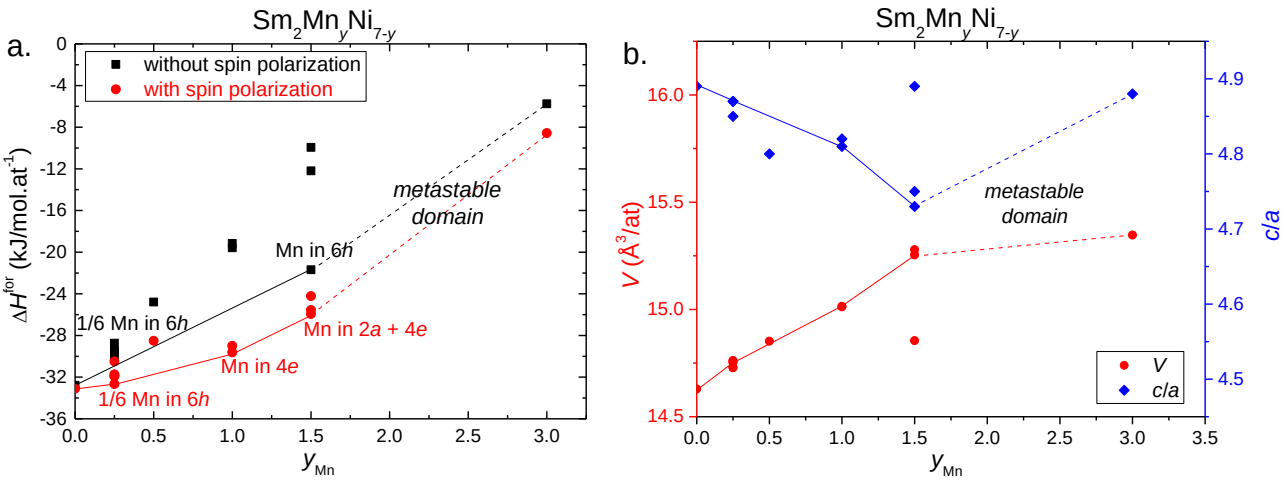

Fig. 7: Investigation of $Sm_2Mn_yNi_{7-y}$ using DFT calculations: (a) heat of formation of every ordered substitution, with and without spin polarization, red and black lines indicate the ground state respectively and (b) the corresponding volume and c/a ratio in 2H Ce_2Ni_7-type structure. A line links the most stable spin-polarization compounds.

$SmMn_yNi_{12-y}$

The experiments were focused on the $SmMn_4Ni_8$ composition. From EPMA (Figure SI-7), it is found that this sample contains $SmMn_{3.7(2)}Ni_{8.3(1)}$ as the main phase. Besides, two secondary phases form with compositions $Sm_2Mn_{4,1(1)}Ni_{12,9(2)}$, attributed to a Th_2Ni_{17}-type compound and $Mn_{40(1)}Ni_{60(1)}$, assigned to a Mn-Ni solid solution. XRD analysis confirms the occurrence of the three phases with 85(2), 5.5(4), and 5.3(1) wt.%, respectively. In addition, a small amount of Sm_2O_3 (<3.9(1) wt. %) is also observed.

Taking advantages of the contrast given for Mn to Ni by AXRD, two patterns collected at 6 and 6.52 keV were jointly refined, taking into consideration the three available sites for the 3*d* metals in the $ThMn_{12}$-type structure. Results of the joint refinement are given in Table 3 and Fig. SI-8, showing that 83,1 % of Mn is located in site 8*i* (CN14), whereas 16,9 % lies in sites 8*f* and 8*j* (CN12; 7,2 % and 9,7 % respectively).

Table 3: Results of the AXRD analysis of $SmMn_4Ni_8$, obtained by joint refinement of two patterns collected at 6 and 6.52 keV, respectively.

Atom	Wyckoff sites	*x*	*y*	*z*	*Occ.*	Coord.
Sm	2*a*	0	0	0	2	
Ni,Mn	8*f*	¼	¼	¼	7,42(8)Ni+0.58(7)Mn	(CN12 Sm_2B_{10})
Ni,Mn	8*i*	0.3550(5)	0	0	1.35(17)Ni+6.65(17)Mn	(CN14 SmB_{13})
Ni,Mn	8*j*	0.2807(4)	½	0	7,23(9)Ni+0.77(9)Mn	(CN12 Sm_2B_{10})

ThMn$_{12}$-type structure; *I*4/*mmm*; *a* = 8.4853(2)Å, *c* = 4.7655(1)Å

The DFT calculation was done for all ordered compounds by the distribution of Ni and Mn in the three available Wyckoff sites. With the same conditions as that of the $Sm_2Mn_yNi_{7-y}$ study, the heats of formation of $SmMn_yNi_{12-y}$ compounds are given in Fig. 88. Again, the magnetic contribution is not negligible since the ΔH^{for} of $SmMn_4Ni_8$ changes from -4.4 to -14.6 kJ mol^{-1} with the ferromagnetic ordering. The larger 8*i* site (CN14) is preferred for Mn in comparison with the two other CN12 sites. In fact, the volume increases up to $y_{Mn} = 4$. For concentrations with $y_{Mn} > 4$, the compounds look unstable with Mn located in CN12 accompanied with an almost positive ΔH^{for} for the binary Sm-Mn compound.

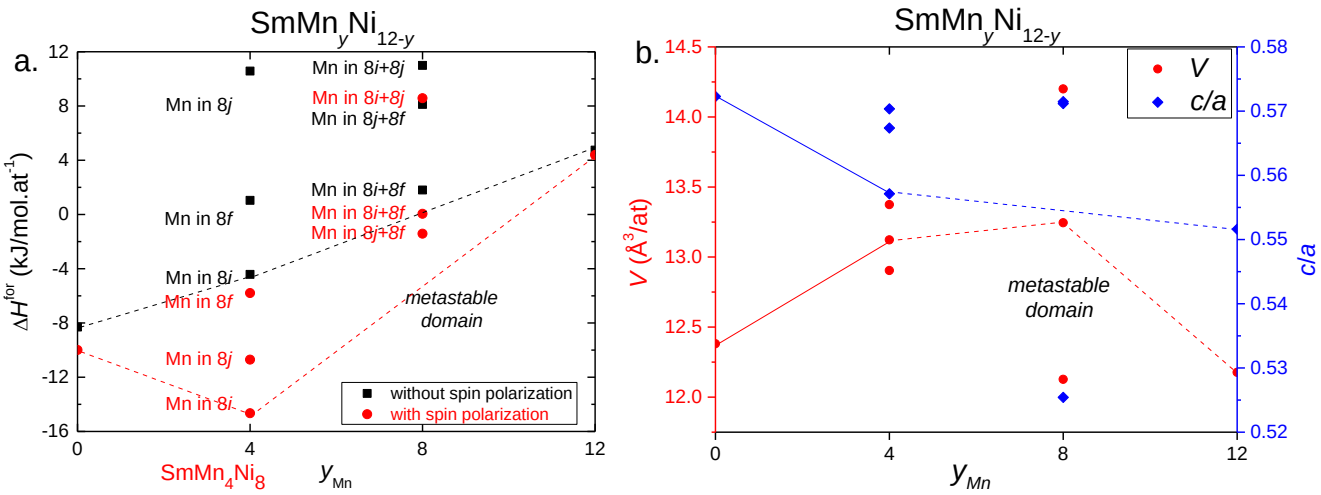

Fig. 8: Investigation of $SmMn_yNi_{12-y}$ using DFT calculations: (a) heat of formation of every ordered substitution, with or without spin polarization, black and red lines indicate the ground state respectively and (b) the corresponding volume and c/a ratio. A line links the most stable spin-polarization compounds.

$Sm_6Mn_yNi_{23-y}$

The EPMA analysis shows the composition $Sm_{5.87(2)}Mn_{23.13(2)}$ as the main phase (Figure SI-9), with some inclusions of a Mn-rich phase ($Mn_{92}Sm_7$). This is confirmed by the XRD pattern that can be correctly indexed with a Th_6Mn_{23}-type phase (*Fm*$\bar{3}$*m*; 94.8(6) wt.%) and a αMn-type *I*$\bar{4}$3*m* secondary phase (5.2 wt.%). Cell parameters are given in Table 1. With a similar approach than the two other families of compound ($Sm_2Mn_yNi_{7-y}$ and $SmMn_yNi_{12-y}$), the DFT investigation on every $Sm_6Mn_yNi_{23-y}$ configurations by the distribution of Mn and Ni in each Wyckoff sites of Th_6Mn_{23} prototype was considered. The results shown in Fig. indicate that Mn presents a site preference for 4*a* and 24*d*. However, the expected binary Sm_6Mn_{23} compound is calculated within our approximation with a positive heat of formation and should thus decomposes in pure elements.

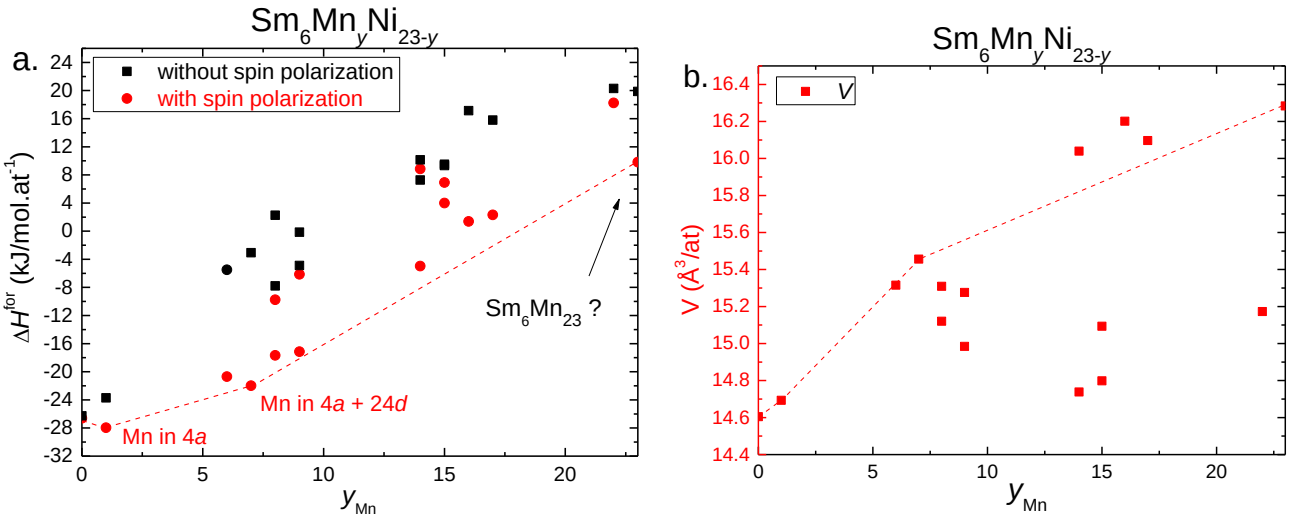

Fig. 9: Investigation of $Sm_6Mn_yNi_{23-y}$ using DFT calculations: (a) heat of formation of every ordered substitution, with or without spin polarization, black and red lines indicate the ground state respectively and (b) the corresponding volume. A line links the most stable spin-polarization compounds.

X-ray absorption spectra have been measured for $Sm_2Mn_yNi_{7-y}$ (y_{Mn} = 0.12, 0.32, 0.49 and 1.0) and SmMn4Ni8 compounds at the Mn K-edge, and the normalized curves are presented in Fig. 10-a. All spectra have very similar shape, and the Mn K-edge position (maximum of the first derivative) located at E0 = 6540 eV is not shifted compared to that of a pure metallic Mn foil. This confirms the metallic state of Mn in the alloys and the similarity of their XANES contributions indicates close local environments for all alloys. The first noticeable difference is the intensity of the small structure at 6542 eV, which increases with the Mn content (Fig. 10-b). Then the small variations of the shape of the spectra between 6545 eV and 6565 eV suggest small changes in the average local and electronic structures upon Mn substitution.

The XAS near edge structure at the Mn-K edge probes the empty projected local electronic density of *p* states. The 4*p* states are hybridized to the 3*d* ones, which are partially empty. Such shoulder 2-3 eV above E_0 have been already observed for other transition metals [29,30], as well as for AB_n intermetallic compounds [28–30] and has been attributed to *p-d* hybridization with *B* neighbors. Upon hydrogenation the intensity of this shoulder decreases due to the apparition of antibonding states which reduce the 4*p* unoccupied DOS near the Fermi level E_F and increase the 3*d* density of state.

In this study this shoulder intensity evolution shows an opposite effect compared to hydrogenation as it increases with Mn concentration. It can therefore be related to an augmentation of the empty *p-d* states with the Mn content. As Mn atoms contains less 3*d* electrons than Ni atoms (-3e$^-$), it is coherent that the percentage of empty *d* state becomes larger upon Mn for Ni substitution. This can be observed in the comparison of the projected DOS of two compounds with different Mn concentrations and with the ideal $SmMn_4Ni_8$ compounds (see Supplementary information, Figure SI-6).

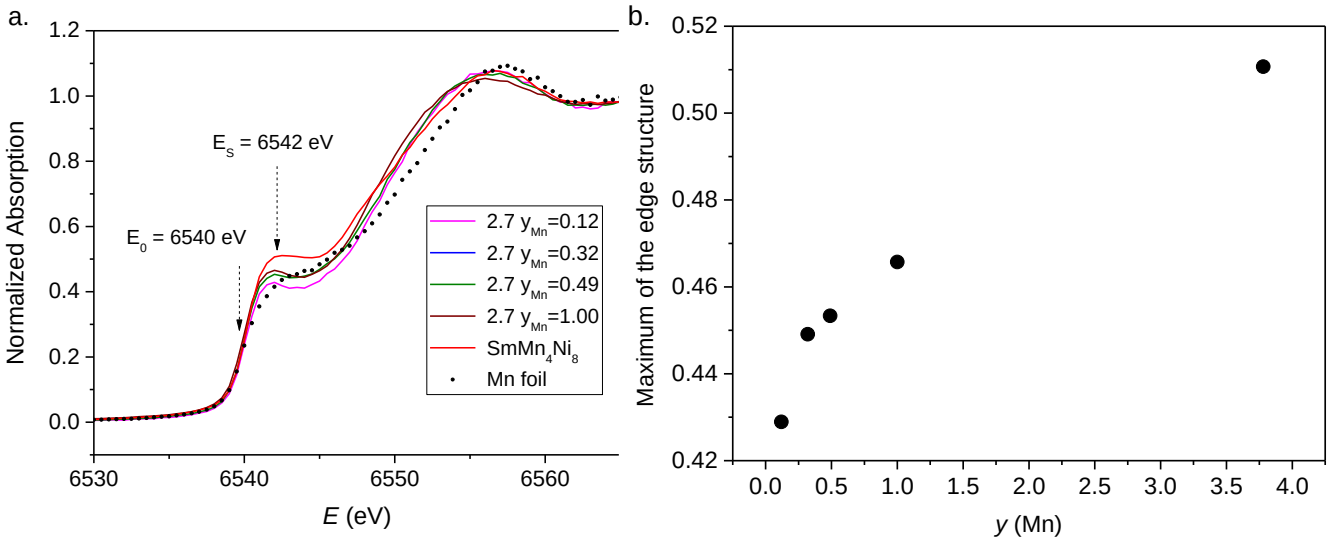

Fig. 10. *(a) X-ray absorption spectra measured at the Mn K-edge for all compounds with stoichiometry Sm2MnyNi7−y (yMn = 0.12, 0.32, 0.49 and 1.0) and SmMn4Ni8 and (b) maximum of the structure at ES as a function of the Mn substitution rate in the compounds.*

Discussions

All compositions targeted in this study ($Sm_2Mn_yNi_{7-y}$; $SmMn_yNi_{12-y}$ and Sm_6Mn_{23}) have been successfully synthesized in agreement with the ternary phase diagram at 400/600 °C published by Bodak *et al.* [9] (Figure 1). For the A_2B_7 system (*A* = Sm, *B* = Mn, Ni), two polymorphs (*R* and *H*) are observed, beside small amounts (<3 wt.%) of samarium oxides. For y_{Mn} = 0.49, the $SmNi_3$-type phase is observed (31(1) wt.%), whereas for y_{Mn} = 1.0, the $SmMnNi_4$ phase appears (14 wt.%). These phases are predicted by the phase diagram [9] and the formation of $SmNi_3$-type has been already reported for y_{Mn} = 0.49 [13].

The data analysis of $Sm_2Mn_yNi_{7-y}$ compounds has shown that when the Mn concentration increases, the Ni atoms are preferentially substituted by Mn in the 6*h* (AB_5 sub-units). Then Mn progressively fills the 12*k* sites (AB_5/AB_2 interface) leading to an increase of the AB_5 sub-unit volume up to *y* = 0.49 followed by a saturation for *y* = 1. Besides, Sm vacancies are found in the $4f_1$ site belonging to the AB_2 sub-units, which cell volume consequently decreases versus the rate of vacancies. This agrees with the presence of *R* vacancies in $R_{1-x}Ni_2$ compounds to relax the geometric constraint induced by r_A/r_B large size effect. Finally, these two antagonist geometric effects first lead to a dilatation (Mn substitution) and then to a contraction (Sm vacancies) of the total cell volume versus y_{Mn} (Fig. 6-b In the present case, the preferential occupancy of Mn atoms for the AB_5 sub-unit has been confirmed thanks to AXRD. Furthermore, the Sm sub-occupancy in *AB*2 sub-units leading to antagonist cell volume variations has been accounted for.Such adversarial effects have been previously observed in other systems and were ascribed to unequal repartition of the substituting element within the sub-units [13,31,32]. In addition, a linear correlation seems to exist between Sm sub-occupancy and Mn substitution as demonstrated in Fig. 3. Evolution of the Sm stoichiometry (x_{Sm}) as a function of the Mn content (y_{Mn}) for the system Sm2MnyNi7−y obtained by EMPA (open squares) and XRD refinement (blue hexagons for 2H and red triangles for 3R). . Therefore, we hypothesize that the structure compensates the volume increase induced by Mn substitution by decreasing the Sm stoichiometry. Possible antisite formation (i.e., occupation of Sm site by Mn atoms) cannot be ruled out but remains beyond the scope of current data analysis.

Another interesting observation is the linear increase of the $H/(H+R)$ ratio versus y_{Mn} (Fig. -a). The coexistence of the *R* and *H* polymorphs is well known in those systems and attributed to geometrical effect related to the atomic sizes [33]. Smaller *A* atoms (i.e., lighter rare earths) are known to stabilize the rhombohedral structure at the expense of the hexagonal one. Substitution of Ni by larger Mn atoms leads to larger *B* atoms with the inverse geometrical effects [13]. The stabilization of the hexagonal phase by Mn substitution has also been previously observed for $La_{1-x}Mg_x(Ni_{1-y}Mn_y)_3$ compounds [34] and $LaY_2Ni_{10.5-x}Mn_x$ alloys [35]. The increase of Sm vacancies, i.e. a decrease of the average *A* size, was expected to stabilize the rhombohedral polymorph, but this is not the case. These results confirm that the Mn for Ni substitution has a dominating effect on the stabilization of the hexagonal phase, and that the Sm vacancies are rather favored to release the stress created by the Mn for Ni substitution. The increase of the $H/H+R$ ratio with Mn content is probably not a pure geometric effect, as the percentage of rhombohedral phase increases upon Ni substitution by larger Al atoms in $LaY_{1.9}Ni_{10.2-x}Al_xMn_{0.5}$ system [36].

Our study also confirms the existence of the $SmMn_4Ni_8$ phase despite the occurrence of small amounts (~5 wt.%) of two secondary phases (Th_2Ni_{17}-type and Mn-Ni solid solution, in line with the ternary phase diagram). The Mn distribution is clearly preferred for the CN14 8*i* site (83 at.%) that offers more room to fit the manganese atoms, larger than the Ni ones. However, 7 to 9 % of the Mn atoms still lie in the CN12 sites. Such results can be compared to those recently published by Belan et al. for $SmMn_{6.8}Ni_{5.2}$ [37]. They confirm the existence of this $ThMn_{12}$-type phase with a cell volume higher than for $SmMn_4Ni_8$ (364,1 for $y_{Mn} = 6.8$ *vs* 343,1 $Å^3$ for $y_{Mn} = 4$; Fig. 2). In addition, they found the site CN14 8*i* is 100% occupied by Mn, while the sites CN12 8*f* and 8*j* are 24 and 46% occupied by Mn, respectively. These results might be taken cautiously as single-crystal X-ray data were used for the structural determination with low contrast between Mn and Ni compared to the present work (done by AXRD). However, they led to the same conclusions regarding the preferred occupation of site 8*i* by Mn atoms. This tendency is confirmed by the DFT calculations, assessing the more stable phase for $y_{Mn} = 4$ and Mn lying only in the CN14 8*i* site.

It is also interesting to look at the overall cell volume evolution of the $SmMn_yNi_{12-y}$ system as a function of the Mn content (Fig. 2). A quasi-linear increase of the cell volume is observed in the range $4 \leq y_{Mn} \leq 8$, in agreement with the DFT calculations that predict a decrease of the volume in the same composition range (Fig. 8) in the non-metastable domain. For $y_{Mn} > 8$, a quasi-plateau is observed, indicating that the substitution of Mn in $SmMn_yNi_{12-y}$ does not occur for higher y_{Mn} values.

The Sm_6Mn_{23} is a well described compound in the literature [39–43]. The compound is indeed observed in the present work forming a binary cubic almost single phase, adopting the Th_6Mn_{23}-type structure. Chemical analysis shows a slight sub-stoichiometry in Sm (Table 1) but this is not confirmed by X-ray diffraction leading to a stoichiometric compound with $a = 12.5896(2)$ Å in agreement with the literature. However, the DFT calculation presents a positive formation energy of binary Sm_6Mn_{23} (+9.81 kJ/mol) leading to its decomposition in pure elements. This result, in agreement with another calculation (+15.82 kJ/mol) [44], raises the problem of calculation for rich-Sm compounds where simple GGA present limitations. In fact, several attempts of non-collinear spin polarization calculations were tried but not successful and probably other exchange and correlation functions should have been tested, as Hubbard contribution, to correctly describe the localized *f*-electron to obtain a stable compound. However, one the Sm-Ni binary side, all the compounds are correctly predicted as expecting from the known phase diagram. In fact, Sm_2Ni_{17}, $SmNi_5$ and Sm_2Ni_7 are on the DFT ground state, where the metastable $SmNi_{12}$ and Sm_6Ni_{23} are not (see Fig SI 10).

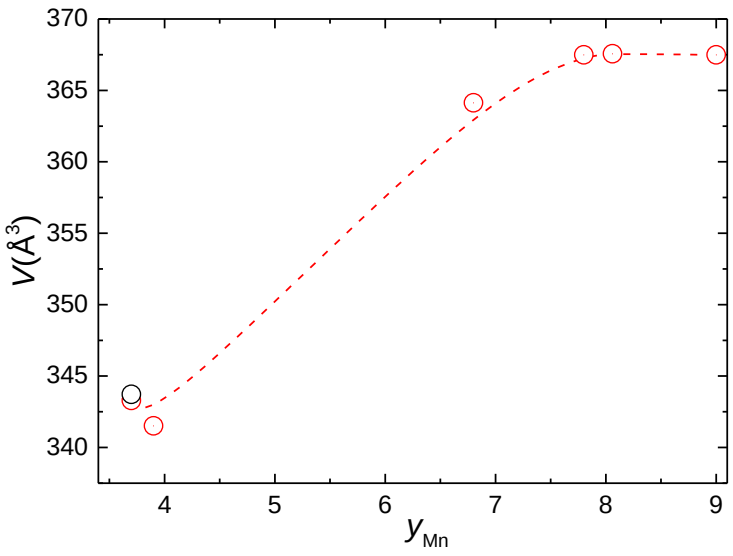

Fig. 2: Cell volume evolution of the $SmMn_yNi_{12-y}$ system as a function of the Mn content in the range $4 \leq y_{Mn} \leq 9$. Data obtained from this work (black circle) and from Belan, Bodak, Kalychak et al. [9,12,37,38] (red circles).

Conclusions

By combining different characterization techniques (standard X-ray diffraction, AXRD, XANES, EPMA) and DFT calculations, the site preference for Ni substitution by Mn atoms in the systems $Sm_2Mn_yNi_{7-y}$ and $SmMn_yNi_{12-y}$ has been clarified. As the example of the stacking Sm_2B_7 phase, the Mn atoms are preferentially occupying AB_5 sub-units because of electronic and volume effects. However, due to the competition between Mn atoms introduction and Sm vacancies creation, the substitution behavior is not regular and leads to antagonist effects of the geometrical parameters (cell volumes) and linear variation of the $H/(H+R)$ ratio for the A_2B_7-type phases. A significant sub-stoichiometry in rare earth (Sm) is also reported for this latter phase and has been successfully assigned to the Mn substitution rate. About the study on $SmMn_yNi_{12-y}$, mainly focused on $SmMn_4Ni_8$ region, the AXRD analysis, in agreement with DFT calculations, shows the Mn preference for the larger 8*i* site (CN14), in comparison with the two other CN12 sites. The Sm_6Mn_{23} existence is experimentally indisputable but its non-stability by DFT is still to be understand. Other phases in equilibrium in the Ni-richer side have been discussed.

Credit authorship contribution statement

Nicolas Madern prepared samples, performed the characterization for $Sm_2(Ni,Mn)_7$ system and participated to AXRD measurements

Judith Monnier prepared samples, performed the characterization for $SmMn_4Ni_8$ compound, participated to AXRD and XANES measurements and analyzed of the XRD and ASD data and led the redaction of the article after the sudden death of M. Latroche

Jean-Claude Crivello performed all the DFT calculations and contributed to the writing and the discussion of the article.

Junxian Zhang prepared samples, performed the characterization for Sm_6Mn_{23} compound, participated to ASD measurements and contributed to the writing and the discussion of the article

Karine Provost participated to AXRD and XANES measurements, analysis of the XANES data and contributed to the writing and the discussion of the article.

Valérie Paul-Boncour participated to AXRD and XANES measurements, analysis of the XANES data and contributed to the writing and discussion of the article.

Solenn Réguer and Dominique Thiaudière are SOLEIL DiffAbs beamline scientist and responsible and were local contacts and enable us to perform the challenging AXRD measurements. In addition, Solenn Reguer gives us plenty of time to help for data extraction.

Michel Latroche participated to AXRD and XANES measurements and analyses of the XRD and AXRD data and lead the redaction of the article until his death on 30th December 2021. This article is dedicated to his memory.

Acknowledgments

We acknowledge SOLEIL facility for provision of synchrotron radiation, and we would like to thank Cristian Mocuta et Philippe Joly for assistance in using beamline DiffAbs. DFT calculations were performed using HPC resources from GENCI-CINES (Grant 2020-096175).

References

[1] W. Hussen, K.-U. Neumann, D.J. Parry, K.R.A. Ziebeck, R. Ballou, J. Deportes, R. Lemaire, B. Ouladdiaf, 3d Magnetism in rare earth intermetallics, Journal of Magnetism and Magnetic Materials. 84 (1990) 281–287. https://doi.org/10.1016/0304-8853(90)90106-Z.

[2] G. Wiesinger, G. Hilscher, Magnetism of hydrides, in: Handbook of Magnetic Materials, K.H.J. Buschow (Ed.), Amsterdam, 2008: pp. 293–456.

[3] K.A. GschneidnerJr, V.K. Pecharsky, A.O. Tsokol, Recent developments in magnetocaloric materials, Rep. Prog. Phys. 68 (2005) 1479–1539. https://doi.org/10.1088/0034-4885/68/6/R04.

[4] V. Paul-Boncour, L. Bessais, Tuning the Magnetocaloric Properties of the La(Fe,Si)13 Compounds by Chemical Substitution and Light Element Insertion, Magnetochemistry. 7 (2021) 13. https://doi.org/10.3390/magnetochemistry7010013.

[5] K.J. Strnat, R.M.W. Strnat, Rare earth-cobalt permanent magnets, Journal of Magnetism and Magnetic Materials. 100 (1991) 38–56. https://doi.org/10.1016/0304-8853(91)90811-N.

[6] V. Yartys, D. Noreus, M. Latroche, Metal hydrides as negative electrode materials for Ni–MH batteries, Appl. Phys. A. 122 (2016) 43. https://doi.org/10.1007/s00339-015-9538-9.

[7] E. Burzo, Hydrogen Storage Materials, Springer; 1st ed. 2018 Edition, Landolt-Börnstein: Numerical Data and Functional Relationships in Science and Technology - New Series (8), 2018.

[8] S. Bobba, S. Carrara, J. Huisman, F. Mathieux, C. Pavel, Critical Raw Materials for Strategic Technologies and Sectors in the EU - A Foresight Study, European Union, 2020. https://doi.org/10.2873/58081.

[9] O.I. Bodak, V.K. Pecharskiy, Y.M. Kalychak, O.I. Kharchenko, I.R. Mokra, L.A. Muratova, D.A. Berezyuk, M.M. Shevchuk, Some ternary systems containing rare earth metals, Fazovye Ravnovesiya Met. Splavakh. (Ed.: M.E. Drits), Izd. Nauka, Moscow, (1981) 57–63.

[10] V. Charbonnier, N. Madern, J. Monnier, J. Zhang, V. Paul-Boncour, Michel. Latroche, Relationship between H2 sorption, electrochemical cycling and aqueous corrosion properties in A_5Ni_{19} hydride-forming alloys (A = Gd, Sm)., J. Power Sources. 397 (2018) 280–287. https://doi.org/10.1016/j.jpowsour.2018.07.033.

[11] J.-C. Crivello, N. Madern, J. Zhang, J. Monnier, M. Latroche, Experimental and Theoretical Investigations on the Influence of A on the Hydrogen Sorption Properties of ANiy Compounds, A = {Y, Sm, Gd}, J. Phys. Chem. C. 123 (2019) 23334–23341. https://doi.org/10.1021/acs.jpcc.9b04600.
[12] Ya.M. Kalychak, O.I. Bodak, E.I. Gladyshevskij, Crystal structure of Ce-Mn-(Fe,Co,Ni) ternary compound systems, Abstracts of Second Vsesoyuznoy Conference on crystal chemistry of intermetallic compounds, Lviv, Ukraine, 1974, 9-10. http://inis.iaea.org/search/search.aspx?orig_q=RN:07275078.
[13] N. Madern, V. Charbonnier, J. Monnier, J. Zhang, V. Paul-Boncour, M. Latroche, Investigation of H Sorption and Corrosion Properties of $Sm_2Mn_xNi_{7-x}$ ($0 \le x < 0.5$) Intermetallic Compounds Forming Reversible Hydrides, Energies. 13 (2020). https://doi.org/10.3390/en13133470.
[14] F.T. Parker, H. Oesterreicher, Intrinsic hardness and mictomagnetism in selected $RMn_{5c}Ni_{5-5c}$ (R=rare earth), J. Magn. Magn. Mat. 36 (1983) 195–207.
[15] J. Zhang, V. Charbonnier, N. Madern, J. Monnier, M. Latroche, Improvement of reversible H storage capacity by fine tuning of the composition in the pseudo-binary systems $A_{2-x}La_xNi_7$ (*A* = Gd, Sm, Y, Mg), Journal of Alloys and Compounds. 852 (2021) 157008. https://doi.org/10.1016/j.jallcom.2020.157008.
[16] J. Rodriguez-Carvajal, Fullprof: a program for Rietveld refinement and pattern matching analysis, Physica B. 192 (1993) 55–69.
[17] Bruker, Bruker AXS (2008): TOPAS V4 : General profile and structure analysis software for powder diffraction data. - User's Manual, Bruker AXS, Karlsruhe, Germany, 2008.
[18] A.A. Coelho, J. Evans, I. Evans, A. Kern, S. Parsons, The TOPAS symbolic computation system, Powder Diffraction. 26 (2011) S22–S25. https://doi.org/10.1154/1.3661087.
[19] A. Michalowicz, J. Moscovici, D. Muller-Bouvet, K. Provost, MAX: multiplatform applications for XAFS, Journal of Physics: Conference Series. 190 (2009) 012034. https://doi.org/10.1088/1742-6596/190/1/012034.
[20] P.E. Blöchl, Projector augmented-wave method, Phys. Rev. B. 50 (1994) 17953–17979. https://doi.org/10.1103/PhysRevB.50.17953.
[21] G. Kresse, J. Furthmüller, Efficient iterative schemes for ab initio total-energy calculations using a plane-wave basis set, Phys. Rev. B. 54 (1996) 11169–11186. https://doi.org/10.1103/PhysRevB.54.11169.
[22] G. Kresse, D. Joubert, From ultrasoft pseudopotentials to the projector augmented-wave method, Phys. Rev. B. 59 (1999) 1758–1775. https://doi.org/10.1103/PhysRevB.59.1758.
[23] J.P. Perdew, K. Burke, M. Ernzerhof, Generalized Gradient Approximation Made Simple, Phys. Rev. Lett. 77 (1996) 3865–3868. https://doi.org/10.1103/PhysRevLett.77.3865.
[24] P.E. Blöchl, O. Jepsen, O.K. Andersen, Improved tetrahedron method for Brillouin-zone integrations, Phys. Rev. B. 49 (1994) 16223–16233. https://doi.org/10.1103/PhysRevB.49.16223.
[25] L. Vegard, Die Konstitution der Mischkristalle und die Raumfüllung der Atome, Z. Phys. Chem. Neue Folge. 5 (1921) 17–26. https://doi.org/10.1007/FBF01349680.
[26] V. Paul-Boncour, J.-C. Crivello, N. Madern, J. Zhang, L.V.B. Diop, V. Charbonnier, J. Monnier, M. Latroche, Correlations between stacked structures and weak itinerant magnetic properties of $La_{2-x}Y_xNi_7$ compounds, Journal of Physics: Condensed Matter. 32 (2020) 415804. https://doi.org/10.1088/1361-648x/ab9d4c.
[27] J.-C. Crivello, J. Zhang, M. Latroche, Structural Stability of ABy Phases in the (La,Mg)–Ni System Obtained by Density Functional Theory Calculations, J. Phys. Chem. C. 115 (2011) 25470–25478. https://doi.org/10.1021/jp204835z.
[28] V. Paul-Boncour, A. Percheron-Guegan, The influence of hydrogen on the magnetic properties and electronic structures of intermetallic compounds: YFe2-D2 system as an example, J. Alloys Compd. 293–295 (1999) 237–242.
[29] B. Lengeler, R. Zeller, X-ray absorption near-edge structure of metal hydrides, Journal of the Less Common Metals. 103 (1984) 337–347. https://doi.org/10.1016/0022-5088(84)90257-1.
[30] N. Ishimatsu, T. Shichijo, Y. Matsushima, H. Maruyama, Y. Matsuura, T. Tsumuraya, T. Shishidou, T. Oguchi, N. Kawamura, M. Mizumaki, T. Matsuoka, K. Takemura, Hydrogen-induced modification of

the electronic structure and magnetic states in Fe, Co, and Ni monohydrides, Phys. Rev. B. 86 (2012) 104430. https://doi.org/10.1103/PhysRevB.86.104430.
[31] V. Berezovets', R. Denys, I.Y. Zavaliy, Crystal structure and thermodynamic properties of YNi2.67Mn0.33H4 hydride, Ser. Khim. 49 (2008) 121–127.
[32] V. Charbonnier, N. Madern, J. Monnier, J. Zhang, V. Paul-Boncour, M. Latroche, Thermodynamic and corrosion study of Sm1-xMgxNiy (y = 3.5 or 3.8) compounds forming reversible hydrides, International Journal of Hydrogen Energy. 45 (2020) 11686–11694. https://doi.org/10.1016/j.ijhydene.2020.02.073.
[33] K.H.J. Buschow, A.S. Van der Goot, Crystal structure or rare earth nickel compounds of the type R2Ni7, J. Less-Common Met. 22 (1970) 419–428.
[34] R.V. Denys, B. Riabov, V.A. Yartys, R.G. Delaplane, M. Sato, Hydrogen Storage Properties and Structure of La1−xMgx(Ni1−yMny)3 Intermetallics and Their Hydrides, J. Alloys Compd. (2007) 446–447, 166–172. https://doi.org/10.1016/j.jallcom.2006.12.137.
[35] W. Xiong, H. Yan, L. Wang, V. Verbetsky, X. Zhao, S. Mitrokhin, B. Li, J. Li, Y. Wang, Characteristics of A2B7-type LaYNi-based hydrogen storage alloys modified by partially substituting Ni with Mn, International Journal of Hydrogen Energy. 42 (2017) 10131–10141. https://doi.org/10.1016/j.ijhydene.2017.01.080.
[36] L. Wang, X. Zhang, S. Zhou, J. Xu, H. Yan, Q. Luo, Q. Li, Effect of Al content on the structural and electrochemical properties of A2B7 type La–Y–Ni based hydrogen storage alloy, International Journal of Hydrogen Energy. 45 (2020) 16677–16689. https://doi.org/10.1016/j.ijhydene.2020.04.136.
[37] B. Belan, D. Kowalska, M. Manyako, M. Dzevenko, Y. Kalychak, Single-crystal investigation of the compound $SmNi_{5.2}Mn_{6.8}$, Zeitschrift Für Naturforschung Section B-A Journal of Chemical Sciences. 75 (2020) 303–307. https://doi.org/10.1515/znb-2019-0181.
[38] Ya.M. Kalychak, O.I. Bodak, E.I. Gladyshevskij, Compounds of the $ThMn_{12}$ type in the Ce - Mn - (Fe, Co, Ni) systems, Sov. Phys. Crystallogr. 21 (1976) 280–282.
[39] K.H.J. Buschow, Magnetic properties of the ternary hydrides of Nd6Mn23 and Sm6Mn23, Solid State Communications. 40 (1981) 207–210. https://doi.org/10.1016/0038-1098(81)90741-9.
[40] P. Lemoine, A. Vernière, T. Mazet, B. Malaman, Magnetic and magnetocaloric properties of R_6Mn_{23} (R=Y, Nd, Sm, Gd-Tm, Lu) compounds, Journal of Magnetism and Magnetic Materials. 323 (2011) 2690–2695. https://doi.org/10.1016/j.jmmm.2011.06.012.
[41] F.T. Parker, H. Oesterreicher, Analysis of magnetic interactions and structure in R6Mn23, Applied Physics A. 27 (1982) 65–69. https://doi.org/10.1007/BF01197548.
[42] F.W. Richter, J. Schütt, Measurement of the local magnetic field, at the site of Sm in Sm6Mn23 by the spin precession method, Zeitschrift Für Naturforschung A. 26 (1971) 1563–1566. https://doi.org/10.1515/zna-1971-1002.
[43] W. Zarek, M. Pardavi-Horvath, Z. Obuszko, Magnetic behaviour of Sm6Mn23−xFex compounds, Journal of Magnetism and Magnetic Materials. 21 (1980) 47–50. https://doi.org/10.1016/0304-8853(80)90486-2.
[44] A. Jain, S.P. Ong, G. Hautier, W. Chen, W.D. Richards, S. Dacek, S. Cholia, D. Gunter, D. Skinner, G. Ceder, K.A. Persson, Commentary: The Materials Project: A materials genome approach to accelerating materials innovation, APL Materials. 1 (2013) 011002. https://doi.org/10.1063/1.4812323.

Supplementary Information (SI)

Investigations of the Mn-Ni-Sm ternary system by means of anomalous X-ray diffraction, X-ray absorption and DFT calculations

Nicolas Madern[1], Judith Monnier[*,1], Jean-Claude Crivello[1], Junxian Zhang[1], Karine Provost[1], Valérie Paul-Boncour[1], Solenn Reguer[2], Dominique Thiaudiere[2], Michel Latroche[1]

[1]Univ. Paris-Est Créteil, CNRS, ICMPE, UMR7182, F-94320, Thiais, France

[2]DIFFABS Beamline, Synchrotron SOLEIL, L'Orme Des Merisiers Saint-Aubin, BP 48, 91192, Gif-sur-Yvette Cedex, France

*corresponding author (judith.monnier@cnrs.fr)

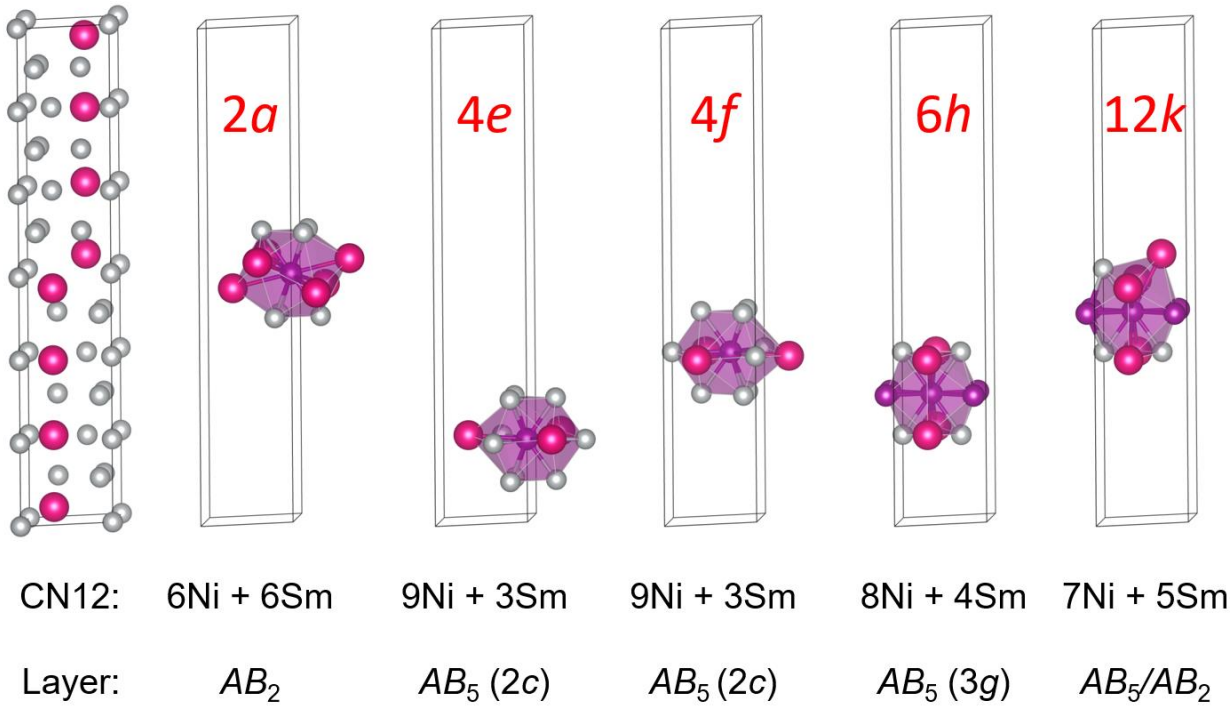

Fig. SI-1: Crystal structure of $SmNi_{12-y}Mn_y$ compounds: Ce_2Ni_7 prototype (hP36), $P6_3/mmc$ (194) on the left with A-type element in pink and B-type element in silver. On the right part: 5 types of crystallographic sites of B-type element, each one has coordination number 12: the central B-type atom is in violet, and surrounded by A-type elements in pink and B-type elements in silver.

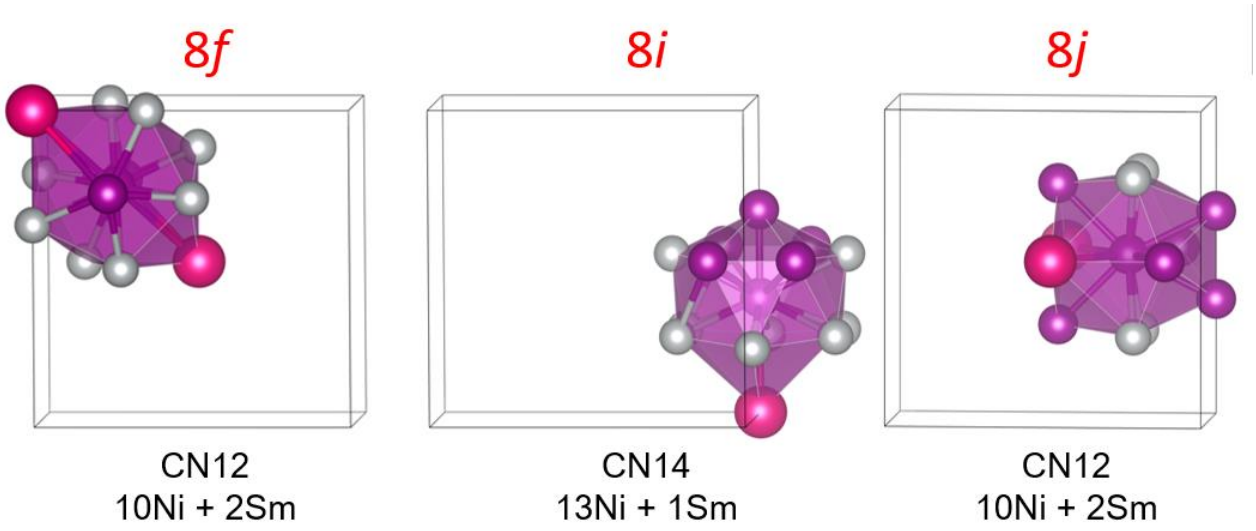

Fig. SI-2: Crystal structure of $SmNi_{12-y}Mn_y$ compounds: $ThMn_{12}$ prototype (tI26), I_4/mmm (139): 3 types of crystallographic sites of B-type element, with two different coordination numbers: the central B-type atom is in violet, and surrounded by A-type elements in pink and B-type elements in silver.

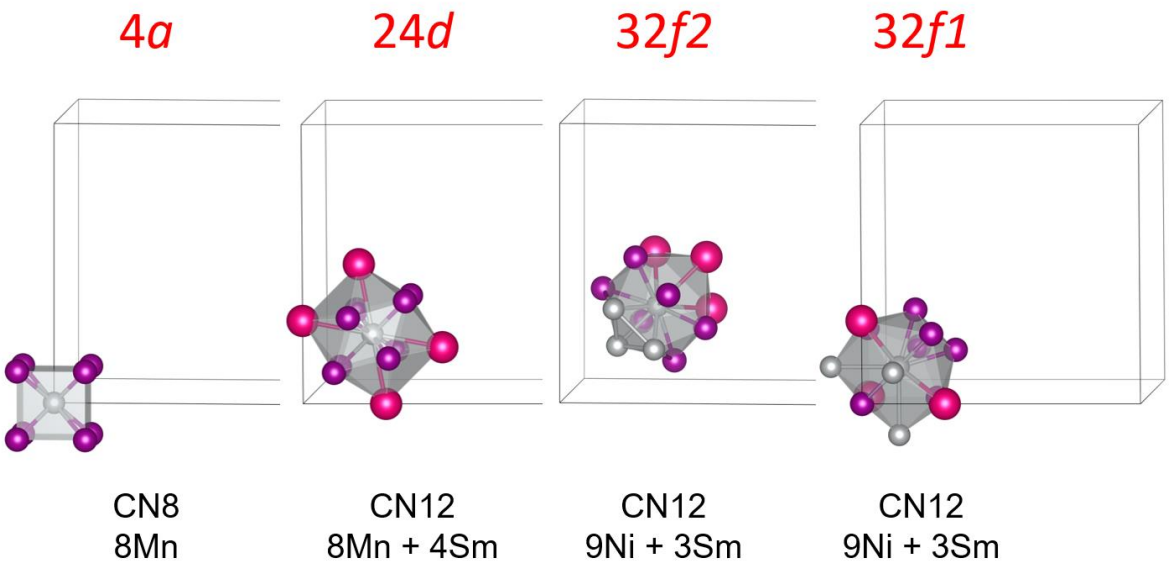

Fig. SI-3: Crystal structure of $Sm_6Ni_{23-y}Mn_y$ compounds: Th_6Mn_{23} prototype (cF116), $Fm\bar{3}m$ (225), 4 types of crystallographic sites of B-type element, with two different coordination numbers: the central B-type atom is in violet, and surrounded by A-type elements in pink and B-type elements in silver.

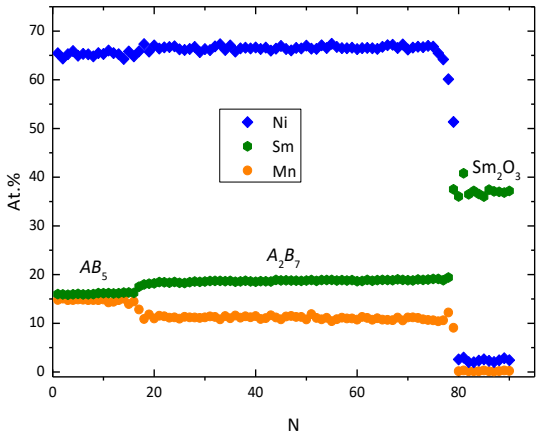

Fig. SI-4: EPMA analysis of $SmMnNi_6$ sample

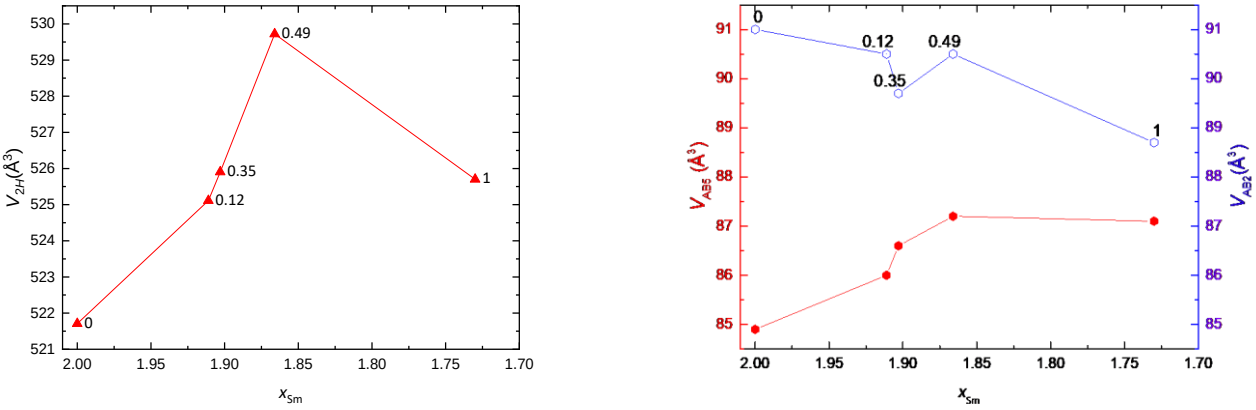

Fig. SI-5: Evolution of (a) the full cell volume and (b) the sub-unit volumes AB_5 (red line) and AB_2 (blue line) as a function of the Sm content x_{Sm} for the system $Sm_xMn_yNi_{7-y}$ with 2H Ce_2Ni_7-type structure. Note that the x-axis decreases from x_{Sm}=2.00 to 1.72 for a better comparison with y_{Mn} (Fig. 6-c)

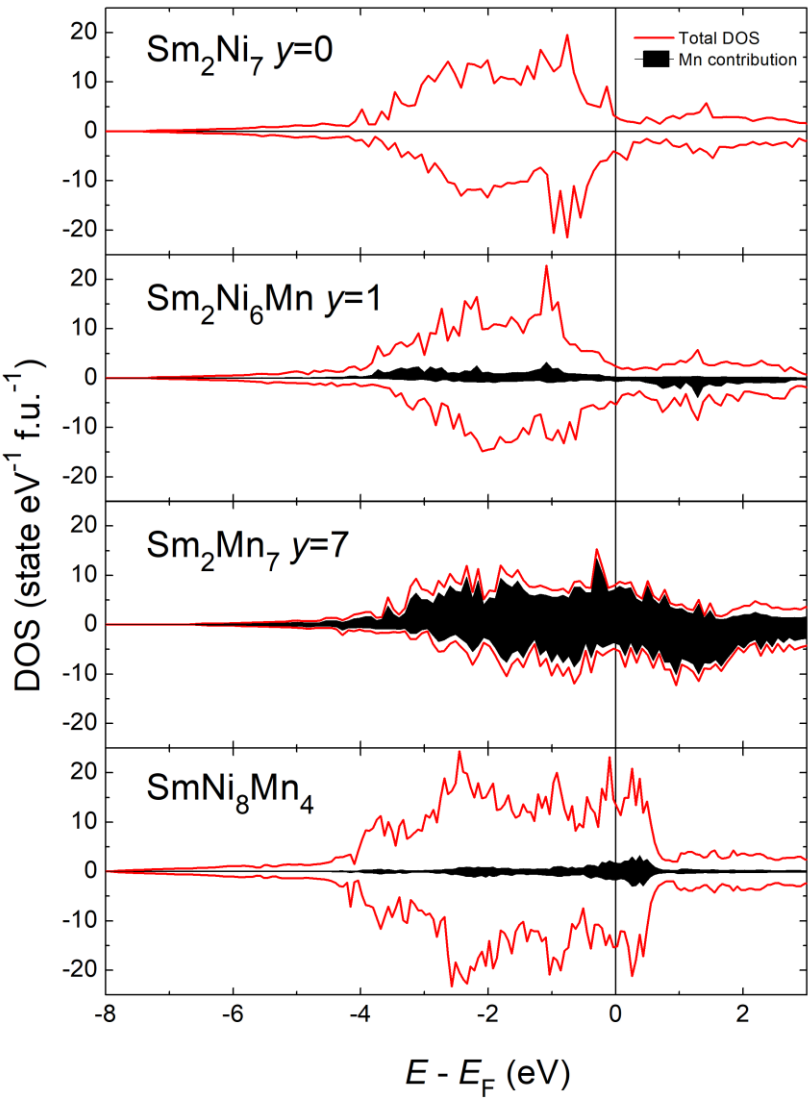

Fig. SI-6: Electronic structure in both spin populations for all $Sm_2Ni_{7-y}Mn_y$ (y = 0, 1, 7) and $SmNi_8Mn_4$ compounds.

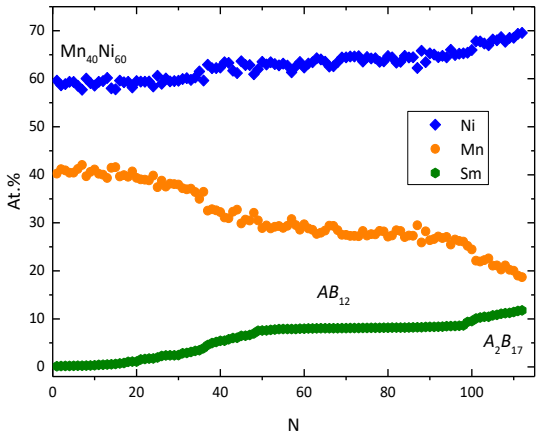

Figure SI-7: EPMA analysis of $SmMn_4Ni_8$

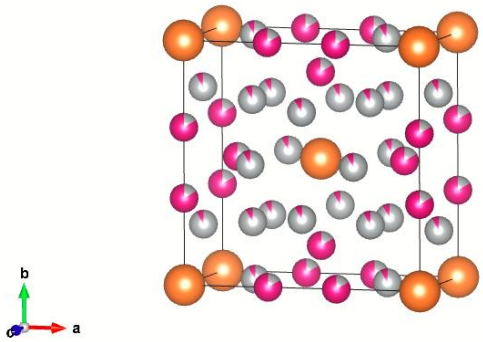

Fig. SI-8: Crystal structure of $SmMn_4Ni_8$ showing the distribution of Mn atoms (violet) in the Ni sites (grey). Samarium is shown as orange spheres ($ThMn_{12}$-type structure; I4/mmm; a= 8.4853(2)Å, c= 4.7655(1)Å)

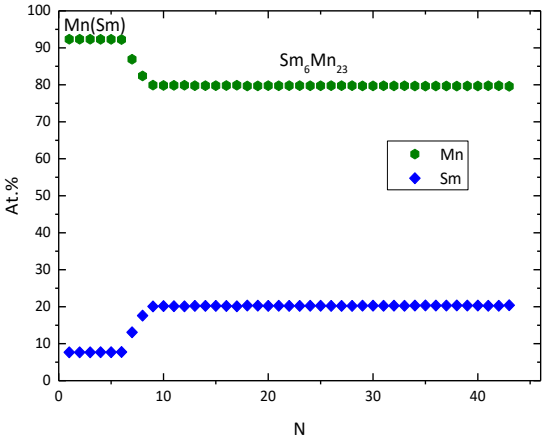

Figure SI-9: EPMA analysis of Sm_6Mn_{23}

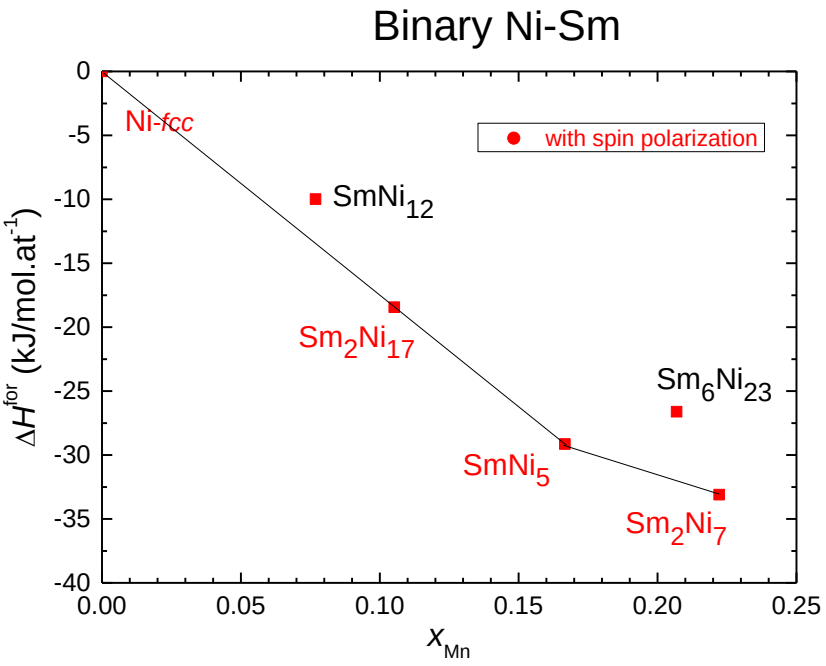

Fig. SI-10: Heat of formation in binary Ni-Sm system (Ni-richer side), lines indicate the ground state